

DOI:10.1002/ejic.201301066

Magnetite/Bi-Doped Carboxylate-Rich Carbon Spheres – A Highly Efficient Magnetic Photocatalyst Based on Dimetallic Fe^{II}/Fe^{III} and Bi^{III}/Bi^{IV} Photoredox Cycles

Zhijun Luo,^[a] Lingling Qu,^[b] Tingting Han,^[b] Zhen Zhang,^[a] Xiaoling Shao,^[a] Xiangyang Wu,^{*[a]} and Zhong-lin Chen^{*[c]}

Keywords: Photooxidation / Redox chemistry / Hydrothermal synthesis / Carbon spheres / Bismuth / Magnetite

A new magnetically separable visible-light photocatalyst, magnetite/Bi-doped carboxylate-rich carbon spheres (Bi-MCRCSSs), was synthesized under ultrasonic irradiation by using magnetite/carboxylate-rich carbon spheres (MCRCSs) as a precursor. The Bi-MCRCSSs showed much better photocatalytic activity than MCRCSs in the degradation of methylene blue (MB) under visible-light irradiation ($\lambda > 420$ nm). Compared with MCRCSs, the Bi-MCRCSSs show more intensive photoabsorption in the whole UV and visible region. In particular, Bi-MCRCSSs display a broad absorption band centered at 550 nm, which give Bi-MCRCSSs advantages over MCRCSs in the utilization of visible light for the degradation of organic pollutants. Owing to the Bi³⁺ doping, the Bi^{III}/Bi^{IV}

redox cycle can be established in the Fe^{II}/Fe^{III} redox cycle system, which result in the establishment of dimetallic Fe^{II}/Fe^{III} and Bi^{III}/Bi^{IV} photoredox cycles for Bi-MCRCSSs. This dimetallic Fe^{II}/Fe^{III} and Bi^{III}/Bi^{IV} photoredox cycle possesses a significantly enhanced photocatalytic degradation rate compared to that of the monometallic photocycles of Fe^{II}/Fe^{III} for MCRCS. The synergistic effects between the Fe^{II}/Fe^{III} cycle and the Bi^{III}/Bi^{IV} cycle promote the regeneration of Fe^{II} ions in Fe^{II}/Fe^{III} cycle and, hence, accelerate the degradation of organic pollutants. In addition, the magnetic saturation (M_s) value is about 20 emu/g. After completion of the reaction, the Bi-MCRCSSs could be rapidly separated under an applied magnetic field.

Introduction

Recently, photo-Fenton systems for wastewater treatment based on ferricarboxylate complexes have attracted much attention because these photo-Fenton systems can utilize natural materials (iron salts and carboxylic acids) and solar energy for the degradation of organic pollutants.^[1–3] Without the use of unstabilized H₂O₂, the combination of carboxylic acids (such as oxalic, malic, citric, and tartaric acids) and iron (just dissolved or as oxides) can form ferricarboxylate complexes that can absorb light irradiation with high quantum yields to trigger radical chain mechanisms of oxidation.^[4–7] Compared with TiO₂-based photocatalytic systems, the iron-based photocatalytic system seems to present more advantages because of the abundance of iron salts in nature and its easy removal from water once used. Iron is the fourth most abundant element

in the Earth's crust and, accordingly, is the most abundant transition metal in soil and plays a central role in many biological and chemical processes. The carboxylate group is one of the most common functional groups in dissolved organic compounds present in natural waters, for example, oxalic acid is mainly secreted by plant roots and coexists in water and soil systems.^[8,9]

Under light irradiation, the carboxylate group can be excited and donate electrons to Fe^{III} species. Therefore, Fe^{III} centers are photoreduced by carboxylate ligands under light irradiation and reoxidized by molecular oxygen, accompanied by the simultaneous oxidation of organic pollutants. Under favorable conditions, complete photodegradation of the organic pollutants can be achieved.^[10,11] In the Fe^{II}/Fe^{III} photoredox cycle under light irradiation, the reduction of Fe^{III} ions to Fe^{II} ions is the rate-limiting step in the overall photo-Fenton reaction. Therefore, the maintenance of a relatively steady Fe^{II} recovery is crucial to accelerate the Fe^{II}/Fe^{III} redox cycles and the oxidation reactivity.^[10,12] By introducing another metal photoredox cycle into the Fe^{II}/Fe^{III} cycle, it can be accelerated and the photo-Fenton reaction rates can be increased; examples of such dimetallic systems consist of Fe and Mn or Fe and Cu.^[11,13]

In our previous work, we presented a visible-light-driven solid-state photo-Fenton reagent based on magnetite/carboxylate-rich carbon spheres (MCRCSs).^[14] The solidification of iron ions and carboxylic acids at the same time was

[a] School of The Environment, Jiangsu University, Zhenjiang 212013, P. R. China
E-mail: wuxy@ujs.edu.cn
http://hjxy.ujs.edu.cn/eng_new/

[b] School of Chemistry and Chemical Engineering, Jiangsu University, Zhenjiang 212013, P. R. China

[c] State Key Laboratory of Urban Water Resource and Environment, Harbin Institute of Technology, Harbin 150090, China

Supporting information for this article is available on the WWW under <http://dx.doi.org/10.1002/ejic.201301066>.

realized in the fabrication of the MCRCSs. Carboxylate groups in the amorphous carbon can form complexes with Fe_3O_4 that can produce $\cdot\text{OH}$ radicals under visible-light irradiation. MCRCSs were obtained by a hydrothermal carbonization (HTC) process. The merit of amorphous carbon obtained by the HTC process is that rich functional groups can remain.^[15,16] In this work, we present a facile ultrasonic method for the synthesis of Bi-MCRCSs by using MCRCSs as the precursor. Compared with MCRCSs, Bi-MCRCSs shows more intensive photoabsorption over the whole range of wavelengths investigated, which should be attributed to N doping. Under visible-light irradiation, the incorporation of Bi ensures that the $\text{Bi}^{\text{III}}/\text{Bi}^{\text{IV}}$ redox cycle is introduced into the $\text{Fe}^{\text{II}}/\text{Fe}^{\text{III}}$ redox cycle, and a dimetallic photocatalytic system based on Bi-MCRCSs is formed. The synergistic effects between the $\text{Fe}^{\text{II}}/\text{Fe}^{\text{III}}$ redox cycle and the $\text{Bi}^{\text{III}}/\text{Bi}^{\text{IV}}$ redox cycle lead to relatively steady recovery of Fe^{II} ions in the $\text{Fe}^{\text{II}}/\text{Fe}^{\text{III}}$ cycle and, hence, accelerate the degradation of organic pollutants.

Results and Discussion

Figure 1 (a) presents the typical XRD patterns of the MCRCSs and Bi-MCRCSs. All of the observed peaks in the two patterns can be indexed to the face-centered-cubic phase of Fe_3O_4 (JCPDS card No. 11-0614). No other characteristic peaks such as the impurities of hematite or hydroxides were detected; therefore, the Bi doping did not af-

fect the Fe_3O_4 crystal structure. No obvious carbon diffraction peaks are observed, which suggests that the carbon coating on Fe_3O_4 is amorphous. Raman spectroscopy can be used to establish the graphitic nature of carbon materials. The Raman spectrum (Figure 1, b) of Bi-MCRCSs shows the characteristic wide D and G bands at ca. 1360 and 1580 cm^{-1} , and the large $I_{\text{D}}/I_{\text{G}}$ value (0.7) indicates the low degree of graphitization. The morphologies of the products were detected by SEM. Figure 1 (c and d) are the SEM images of the precursor MCRCSs and Bi-MCRCSs, respectively. From Figure 1 (c), it can be seen that the precursor MCRCSs have a relatively uniform diameter of ca. 4 μm and are composed of a large quantity of small nanoparticles. In comparison with the precursor MCRCSs, some Bi-MCRCSs are cracked, which should be attributed to corrosion caused by HNO_3 and the ultrasonic treatment. Energy-dispersive X-ray spectroscopy (EDS) element mapping of the SEM image (Figure S1) shows that the Fe and Bi are homogeneously distributed throughout the sample. The homogeneous distribution of Fe and Bi on the surface of Bi-MCRCSs is beneficial for the fabrication of a dimetallic photocatalytic system based on $\text{Fe}^{\text{II}}/\text{Fe}^{\text{III}}$ and $\text{Bi}^{\text{III}}/\text{Bi}^{\text{IV}}$ photoredox cycles. Figure S2 shows the TEM image of a broken of Bi-MCRCSs particle. It is clear that the particle is a typical core-shell structure with an Fe_3O_4 core and a carbon shell.

FTIR spectroscopy was used to identify the functional groups present in Bi-MCRCSs. Figure 2 (a) shows the

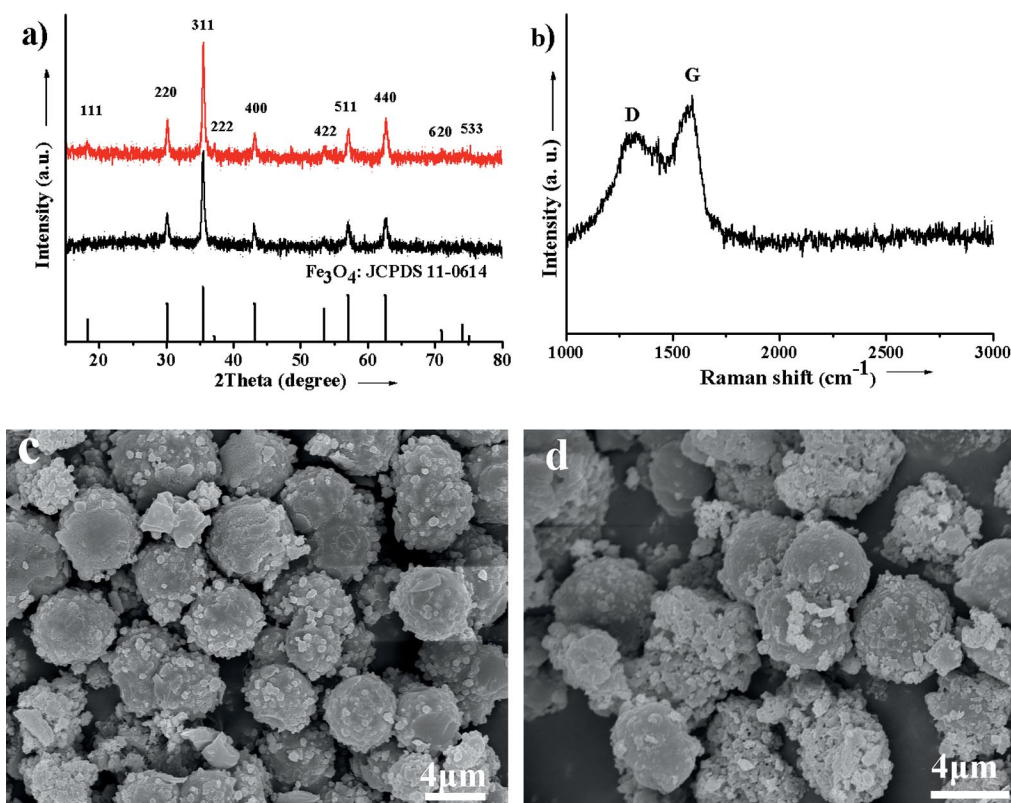


Figure 1. (a) XRD pattern of Bi-MCRCSs and MCRCSs, (b) Raman spectra of Bi-MCRCSs, (c) SEM image of MCRCSs, and (d) SEM image of Bi-MCRCSs.

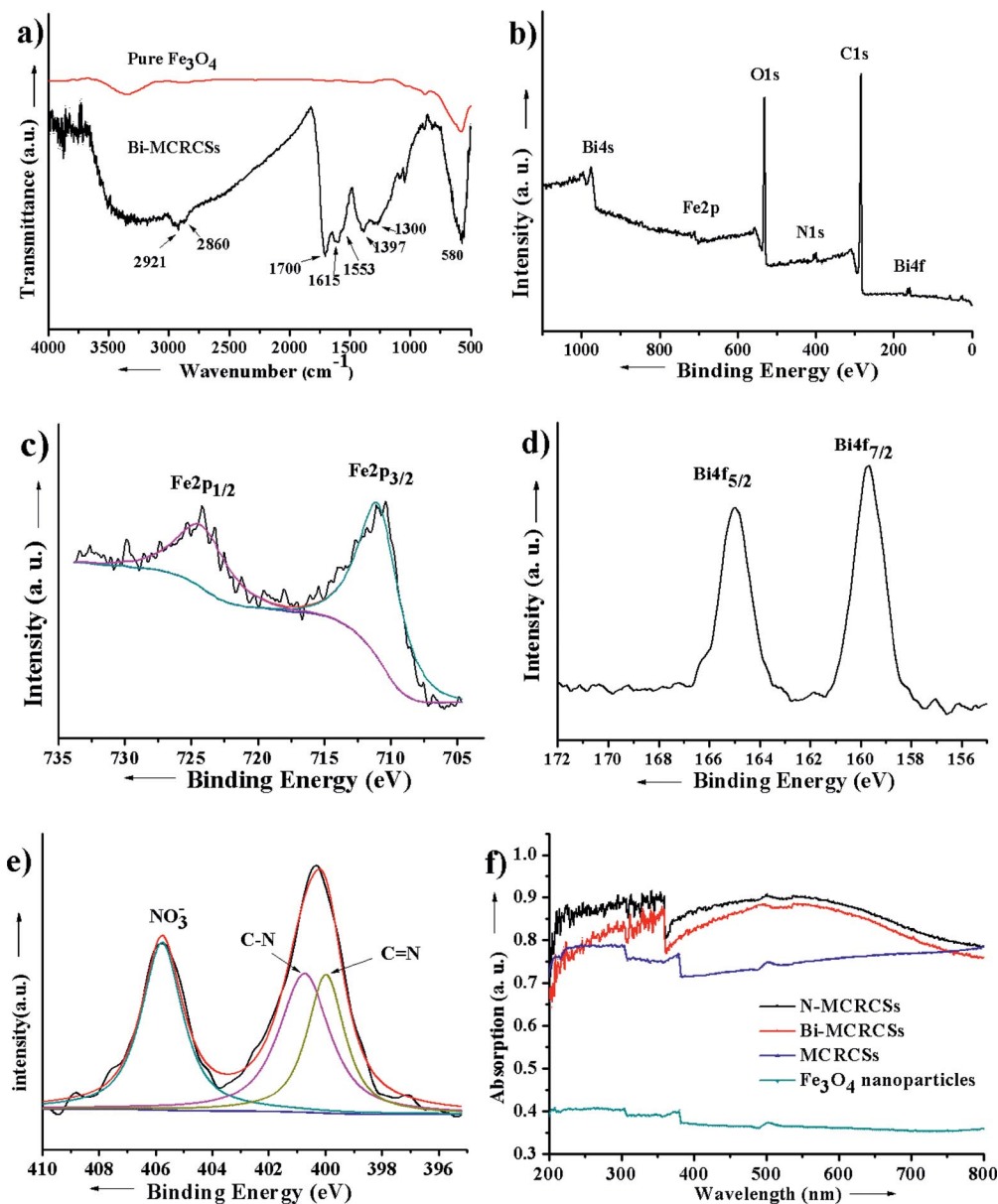


Figure 2. (a) FTIR spectrum of Bi-MCRCSSs; (b–e) XPS spectra of Bi-MCRCSSs, (b) survey scan (c) Fe 2p, (d) Bi 4f, (e) N 1s; (f) UV/Vis absorption spectra of Fe₃O₄ nanoparticles, MCRCSs, N-MCRCSSs, and Bi-MCRCSSs.

FTIR spectra of Fe₃O₄ nanoparticles and Bi-MCRCSSs. The bands at 1700 and 1618 cm⁻¹ are attributed to C=O and C=C vibrations, respectively, which reveals the aromatization of gluconate during the hydrothermal treatment. The appearance of the bands at 1615 and 1397 cm⁻¹ can be assigned to the asymmetric and symmetric stretching vibrations of COO⁻ groups and confirm that large amounts of carboxylate groups from the carbon shell are coordinated strongly to the iron cations.^[17] The band at 3400 cm⁻¹ implies the existence of large numbers of hydroxyl groups. The bands at 2921 and 2860 cm⁻¹ should be attributed to the –CH₂– stretching vibration.^[18] The bands at 1300 and 1553 cm⁻¹ can be assigned to C–N and C=N.^[19] The bands at 580 cm⁻¹ in the FTIR spectra of the Fe₃O₄ nanoparticles and Bi-MCRCSSs are attributed to the Fe–O absorption band.^[20]

To further identify the chemical states of the Fe and Bi in the samples studied, Bi-MCRCSSs were characterized by XPS. Figure 2 (b) shows the different XPS spectral regions that correspond to different elements for the Bi-MCRCSSs. The XPS spectra display the binding energies for Bi (4s), Fe (2p), O (1s), N (1s), C (1s), and Bi (4f) of the Bi-MCRCSSs. In the Fe 2p XPS spectra (Figure 2, c), the peaks for Fe 2p_{3/2} and Fe 2p_{1/2} were observed at 711.2 and 724.5 eV, which is also indicative of the formation of a Fe₃O₄ phase in Bi-MCRCSSs.^[17] Figure 2 (d) depicts two intense peaks for Bi 4f_{7/2} and Bi 4f_{5/2} with binding energies of 159.6 and 164.9 eV, respectively, which are attributable to Bi³⁺ ions.^[21] This demonstrates the successful incorporation of the Bi atoms into the MCRCS precursor. For the N 1s spectra presented in Figure 2 (e), three component peaks with binding energies at ca. 405.8, 401, and 400.1 eV were identified

and are attributed to the NO_3^- , C–N, and C=N bonds, respectively.^[22,23] According to the FTIR and XPS results, it was demonstrated that a large number of carboxylate and hydroxyl groups remained in the Bi-MCRCs. Owing to the strong coordinating ability of carboxylate groups to metal cations, carboxylate groups from the carbon shell were co-ordinated strongly to the iron and bismuth cations to form ferric-carboxylate and bismuth carboxylate complexes, respectively. Figure 2 (f) shows the UV/Vis absorption spectra of the Fe_3O_4 nanoparticles, MRCs, N-MRCs, and Bi-MRCs. Compared with the Fe_3O_4 nanoparticles, MRCs, N-MRCs, and Bi-MRCs all exhibit en-

hanced absorption in the whole UV and visible region, which should be attributed to the carbon coating. N-MRCs and Bi-MRCs shows more intense absorption than MRCs in the whole range of wavelengths investigated. In particular, N-MRCs and Bi-MRCs display a broad absorption band centered at 550 nm. The enhanced absorption of N-MRCs and Bi-MRCs in the whole visible region should be attributed to the N doping. The strong absorption in the visible-light region gives N-MRCs and Bi-MRCs advantages over Fe_3O_4 nanoparticles and MRCs for the utilization of visible light for the degradation of organic pollutants.

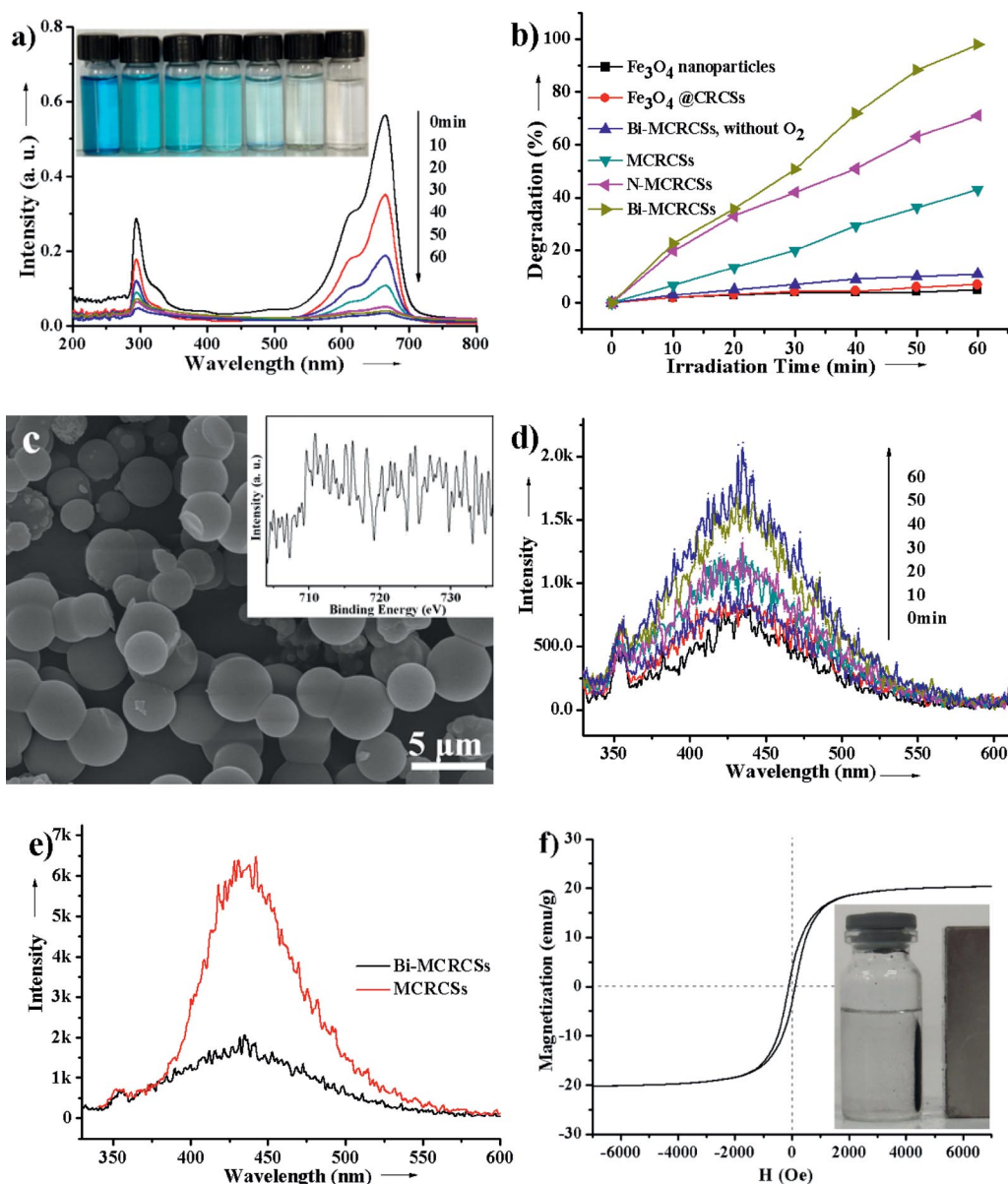


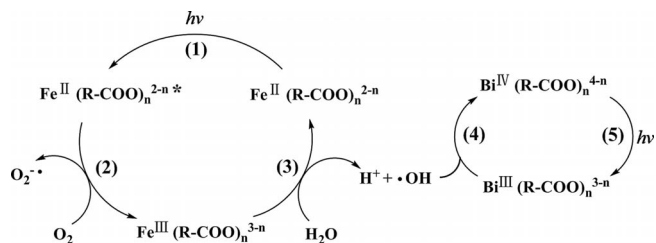
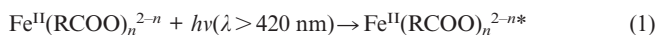
Figure 3. (a) UV/Vis spectra of MB vs. photoreaction time in the presence of Bi-MCRCs; (b) photocatalytic degradation of MB over the Fe_3O_4 nanoparticles, Fe_3O_4 @CRCs, Bi-MCRCs without O_2 , MRCs, N-MCRCs, and Bi-MCRCs; (c) SEM image of Fe_3O_4 @CRCs; the inset is the Fe 2p XPS spectrum of Fe_3O_4 @CRCs; (d) $\cdot\text{OH}$ -trapping PL spectra of Bi-MCRCs/TA solution; (e) $\cdot\text{OH}$ -trapping PL spectra of Bi-MCRCs/TA solution and MRCs/TA solution after 60 min of visible-light irradiation. (f) Field-dependent magnetization curve of Bi-MCRCs at room temperature; the inset shows the strong attraction of the particles suspended in water toward a magnet.

The photocatalytic activity of the Bi-MCRCSSs was evaluated by the degradation of methylene blue (MB) in water under visible-light irradiation ($\lambda > 420$ nm) at room temperature. The main absorption peak of MB at 665 nm was used to monitor the photocatalytic degradation process. Figure 3 (a) presents the UV/Vis spectra of an aqueous MB solution irradiated by visible light with Bi-MCRCSSs as photocatalyst over various time intervals. The Bi-MCRCSSs exhibit a surprising degradation of MB under visible-light irradiation. MB was almost completely degraded after 60 min of visible-light irradiation. No new absorption bands appear in either the visible or the UV region, which indicates the complete photocatalytic degradation of MB. Further experiments were performed to compare the photocatalytic activities of Fe_3O_4 nanoparticles, Fe_3O_4 @CRCSs, Bi-MCRCSSs without O_2 , MCRCSs, N-MCRCSSs, and Bi-MCRCSSs (Figure 3, b). Nearly no degradation of MB was detected under visible-light irradiation when Fe_3O_4 nanoparticles or Fe_3O_4 @CRCSs acted as the photocatalyst. MCRCSs exhibits a higher photocatalytic activity, and the degradation percentage of MB was 43%. In the presence of N-MCRCSSs, MB degradation reached ca. 72% after 60 min of visible-light irradiation because of its strong absorption in the visible-light region. It is clear that Bi-MCRCSSs produce the highest degradation percentage of MB (98%) after 60 min of visible-light irradiation without the use of H_2O_2 ; this value is ca. 2.28 times higher than that of the MCRCSs. The fast photocatalytic degradation rate of MB with Bi-MCRCSSs is possibly attributed to the N and Bi doping. According to the Fe 2p XPS spectrum of Fe_3O_4 @CRCSs (inset of Figure 3, c), no Fe could be found on the surface of Fe_3O_4 @CRCSs obtained by the conventional two steps method, which implies that the Fe_3O_4 nanoparticles were completely coated by carbon. The absence of ferricarboxylate on the surface of Fe_3O_4 @CRCSs means that MB could not be degraded. This result indicates that ferricarboxylate [$\text{Fe}^{\text{II}}(\text{RCOO})_n^{2-n}$ and $\text{Fe}^{\text{III}}(\text{RCOO})_n^{3-n}$] on the surface of MCRCSs, N-MCRCSSs, and Bi-MCRCSSs is responsible for their prominent photocatalytic properties under visible-light irradiation.

Until recently, photo-Fenton chemistry was still far from being fully understood. Generally, the photo-Fenton reaction with monometallic $\text{Fe}^{\text{II}}/\text{Fe}^{\text{III}}$ photocycles has been demonstrated to rapidly degrade many organic compounds with hydroxyl radicals ($\cdot\text{OH}$).^[10] In our previous work, the solidification of iron ions and carboxylic acids at the same time was realized by the fabrication of MCRCSs. Carboxylate groups in the amorphous carbon can form complexes with Fe_3O_4 , which can produce a high concentration of $\cdot\text{OH}$ radicals under visible-light irradiation. The monometallic $\text{Fe}^{\text{II}}/\text{Fe}^{\text{III}}$ photocycle of MCRCS exhibits excellent photocatalytic activity under visible-light irradiation.^[14] According to the XPS results, the Bi^{3+} ions are doped into the MCRCS and the Bi^{3+} ions can easily be oxidized to Bi^{4+} ions by $\cdot\text{OH}$ radicals in the photoredox $\text{Fe}^{\text{II}}/\text{Fe}^{\text{III}}$ cycling system, which will result in the establishment of the dimetallic photoredox $\text{Fe}^{\text{II}}/\text{Fe}^{\text{III}}$ and $\text{Bi}^{\text{III}}/\text{Bi}^{\text{IV}}$ cycles for Bi-MCRCSSs. The enhanced photocatalytic activity of N-

MCRCSs and Bi-MCRCSSs can be attributed to the enhanced absorption in the whole visible region owing to the N doping. According to the results shown in Figure 3 (b), the photocatalytic degradation rate of MB on Bi-MCRCSSs is ca. 1.36 times higher than that of N-MCRCSSs, which should be attributed to the Bi doping. Owing to the Bi doping, the dimetallic $\text{Fe}^{\text{II}}/\text{Fe}^{\text{III}}$ and $\text{Bi}^{\text{III}}/\text{Bi}^{\text{IV}}$ photoredox cycles of Bi-MCRCSSs possess a significantly enhanced photocatalytic degradation rate compared to those of the monometallic $\text{Fe}^{\text{II}}/\text{Fe}^{\text{III}}$ photocycles of MCRCSs and N-MCRCSSs.

A presumable catalytic mechanism for the Bi-MCRCSSs was proposed for the synergistic effects between the $\text{Fe}^{\text{II}}/\text{Fe}^{\text{III}}$ and $\text{Bi}^{\text{III}}/\text{Bi}^{\text{IV}}$ cycles under visible-light irradiation. The catalytic mechanism is summarized in Scheme 1. Carbon materials are often used to enhance the photocatalytic efficiency of catalysts by acting as photosensitizers for visible light.^[24] The carboxylate groups that remain in the carbon are coordinated strongly to Fe_3O_4 and form ferricarboxylate complexes. The $\text{Fe}^{\text{II}}(\text{RCOO})_n^{2-n}$ complexes on the surface of Bi-MCRCSSs are photoexcited by absorption of visible light (designated by an asterisk), see Equation (1).

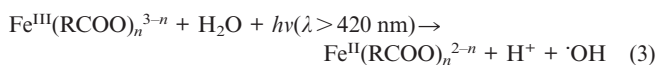


Scheme 1. Proposed dimetallic photoredox cycle for Bi-MCRCSSs.

The $\text{Fe}^{\text{II}}(\text{RCOO})_n^{2-n*}$ transfers an electron to O_2 and produces a superoxide radical anion ($\text{O}_2^{\cdot-}$), see Equation (2).



Further investigation indicates that the Bi-MCRCSSs catalyst exhibits an O_2 -dependent feature in the reaction. In the absence of O_2 , the degradation percentage of MB is only 11% after 60 min of visible-light irradiation (Figure 3, b), which clearly indicates that O_2 is necessary for this reaction system and Bi-MCRCSSs can activate O_2 under mild conditions. Under visible-light irradiation, $\text{Fe}^{\text{III}}(\text{RCOO})_n^{3-n}$ is photoreduced to $\text{Fe}^{\text{II}}(\text{RCOO})_n^{2-n}$ with concomitant production of $\cdot\text{OH}$ radicals, as shown in Equation (3).



The generation of $\cdot\text{OH}$ radicals was investigated by the terephthalic acid photoluminescence probing technique (TAPL), which has been widely used for the detection of

OH radicals.^[25] The terephthalic acid (TA) reacts with the OH radicals to form 2-hydroxyterephthalic acid (HTA) during the photocatalytic process, which can be measured with a fluorescence spectrophotometer as HTA exhibits a strong fluorescence peak ($\lambda_{\text{ex}} = 315 \text{ nm}$, $\lambda_{\text{em}} = 426 \text{ nm}$). Thus, we measured the fluorescence intensity of HTA to detect the OH radicals indirectly. The photoluminescence (PL) spectra of a Bi-MCRCSSs/TA solution under visible-light irradiation are shown in Figure 3 (d). The fluorescence intensity at 426 nm increased steadily with irradiation time, which elucidated that Bi-MCRCSSs could produce OH radicals in situ under visible-light irradiation without the use of H_2O_2 . The photoluminescence spectra of MCRCSs/TA and Bi-MCRCSSs/TA solutions after 60 min of visible-light irradiation are shown in Figure 3 (e). It is clear that the fluorescence intensity of MCRCSs is three times higher than that of Bi-MCRCSSs, which means that the concentration of OH radicals produced by MCRCSs is higher than that produced by Bi-MCRCSSs. However, the photodegradation rate of the Bi-MCRCSSs is 2.28 times higher than that of MCRCSs. According to the results mentioned above, for the dimetallic photoredox $\text{Fe}^{\text{II}}/\text{Fe}^{\text{III}}$ and $\text{Bi}^{\text{III}}/\text{Bi}^{\text{IV}}$ cycles of Bi-MCRCSSs, in the activation of O_2 , O_2 is the main oxidant and the active oxygen species is $\text{O}_2^{\cdot-}$ rather than OH.

In the photo-Fenton catalytic cycle, the photoreduction of Fe^{III} to Fe^{II} is the rate-determining step. Therefore, any strategies to increase the regeneration of Fe^{II} ions will promote the $\text{Fe}^{\text{II}}/\text{Fe}^{\text{III}}$ cycle and, hence, accelerate the degradation of organic pollutants, whereas those that prevent the $\text{Fe}^{\text{II}}/\text{Fe}^{\text{III}}$ cycle will slow down the reaction.^[10,12] In the dimetallic photoredox $\text{Fe}^{\text{II}}/\text{Fe}^{\text{III}}$ and $\text{Bi}^{\text{III}}/\text{Bi}^{\text{IV}}$ cycle, the Bi^{III} ions behave as a good scavenger for OH radicals and are gradually oxidized to Bi^{IV} ions [reaction (4) in Scheme 1]. The Bi^{IV} ions can be reduced by Fe^{II} ions and photoreduced by visible-light irradiation, and the $\text{Bi}^{\text{III}}/\text{Bi}^{\text{IV}}$ cycle is realized. The scavenging of OH radicals by Bi^{III} ions is propitious to make the reaction (3) shift to right and generate more Fe^{II} ions. A similar result was also found in the dimetallic $\text{Fe}^{\text{II}}/\text{Fe}^{\text{III}}$ and $\text{Cr}^{\text{III}}/\text{Cr}^{\text{IV}}$ photoredox cycle, in which Cr^{III} ions are oxidized to Cr^{IV} ions by OH radicals.^[26] The synergistic effects between the $\text{Fe}^{\text{II}}/\text{Fe}^{\text{III}}$ cycle and the $\text{Bi}^{\text{III}}/\text{Bi}^{\text{IV}}$ photocatalytic cycle promote the regeneration of Fe^{II} ions in $\text{Fe}^{\text{II}}/\text{Fe}^{\text{III}}$ cycle and, hence, accelerates the degradation of organic pollutants. To confirm the stability of the high photocatalytic performance of the Bi-MCRCSSs, the circulating runs in the photocatalytic degradation of MB in the presence of Bi-MCRCSSs under visible-light irradiation were checked (Figure S3). After four cycles, the photocatalytic efficiency of the Bi-MCRCSSs decreased by only 11%, which indicates that the Bi-MCRCSSs are highly stable. The magnetic properties of Bi-MCRCSSs were studied by using a superconducting quantum interference device (SQUID) magnetometer at room temperature. Figure 3 (f) displays hysteresis loops of MCRCSs, which indicate that it possesses a magnetic saturation (M_s) value of ca. 20 emu/g. After the completion of the reactions, the Bi-MCRCSSs could be rapidly separated under an applied magnetic field (inset in Figure 3, f).

Conclusion

A simple ultrasonic method was used to fabricate Bi-MCRCSSs by using MCRCSs as a precursor. The dimetallic $\text{Fe}^{\text{II}}/\text{Fe}^{\text{III}}$ and $\text{Bi}^{\text{III}}/\text{Bi}^{\text{IV}}$ photoredox cycles of Bi-MCRCSSs possess a significantly enhanced photocatalytic degradation rate compared to that of the monometallic $\text{Fe}^{\text{II}}/\text{Fe}^{\text{III}}$ photocycles of MCRCS. According to FTIR and XPS results, it was demonstrated that a large number of carboxylate and hydroxy groups remained in the Bi-MCRCSSs, and carboxylate groups from the carbon layer were coordinated strongly to the iron cations, which implies that ferric-carboxylate complexes are formed. Compared with the Fe_3O_4 nanoparticles and MCRCSs, N-MCRCSSs and Bi-MCRCSSs all exhibit enhanced absorption in the whole UV and visible region. The strong absorption in the visible-light region gives N-MCRCSSs and Bi-MCRCSSs advantages over Fe_3O_4 nanoparticles and MCRCSs to utilize visible light for the degradation of organic pollutants. The synergistic effects between the $\text{Fe}^{\text{II}}/\text{Fe}^{\text{III}}$ cycle and the $\text{Bi}^{\text{III}}/\text{Bi}^{\text{IV}}$ photocatalytic cycle promote the regeneration of Fe^{II} ions in $\text{Fe}^{\text{II}}/\text{Fe}^{\text{III}}$ cycle and, hence, accelerate the degradation of organic pollutants. In addition, Bi-MCRCSSs can be easily recycled by applying an external magnetic field.

Experimental Section

Preparation of Magnetite/Carboxylate-Rich Carbon Spheres (MCRCSs): MCRCSs were synthesized by the hydrothermal carbonization (HTC) process. Briefly, FeCl_3 (0.5 g) and sodium gluconate (3 g) were dissolved in deionized water (60 mL), and the solution was transferred into a Teflon[®]-lined stainless-steel autoclave with a capacity of 100 mL. The autoclave was sealed and heated at 180 °C for 24 h. After cooling to room temperature, the black products were washed several times with deionized water and absolute ethanol. Finally, the washed precipitate was dried in a vacuum oven at 60 °C for 12 h.

Preparation of Magnetite/Bi-Doped Carboxylate-Rich Carbon Spheres (Bi-MCRCSSs): $\text{Bi}(\text{NO}_3)_3 \cdot 5\text{H}_2\text{O}$ (0.2 g) was first dissolved in a nitric acid solution (1.2 mol/L, 10 mL) to avoid hydrolysis of the Bi^{3+} ions, and the solution was stirred for 30 min. Then, MCRCSs (0.2 g) were dispersed into the above solution, and the mixture was given a 300 W (40 kHz) ultrasonic treatment for 30 min at room temperature. After that, the black products were washed several times with deionized water and absolute ethanol. Finally, the washed precipitation was dried in a vacuum oven at 60 °C for 12 h, and the Bi-MCRCSSs were obtained.

Preparation of Magnetite/N-Doped Carboxylate-Rich Carbon Spheres (N-MCRCSSs): MCRCSs (0.2 g) were dispersed into a 2 M HNO_3 aqueous solution. The suspension was given a 300 W (40 kHz) ultrasonic treatment for 30 min at room temperature. After that, the black products were washed several times with deionized water and absolute ethanol. Finally, the washed precipitate was dried in a vacuum oven at 60 °C for 12 h, and the magnetite/N-doped carboxylate-rich carbon spheres were obtained.

Preparation of Magnetite@carboxylate-Rich Carbon Spheres by the Conventional Two-Step Method (Fe_3O_4 @MCRCSs): Fe_3O_4 @MCRCSs were synthesized by the conventional two-step method, the synthesis of Fe_3O_4 core and the subsequent coating of carbon shell.

Preparation of Fe₃O₄ Nanoparticles: FeCl₃·6H₂O (2.43 g) and FeSO₄·7H₂O (1.67 g) were dissolved in deionized water (50 mL) under nitrogen gas with vigorous stirring at 80 °C. Then, 2 M NaOH aqueous solutions were rapidly added into the solution until the pH of the solution was adjusted to 10. After heating, the black suspension was cooled to room temperature naturally. The black products were washed several times with deionized water and absolute ethanol. Finally, the washed precipitation was dried in a vacuum oven at 60 °C for 12 h.

Preparation of Fe₃O₄@CRCSs: Fe₃O₄ nanoparticles were first immersed in a 0.1 M HNO₃ solution for 5 min and then separated with a magnet and washed several times with deionized water. Subsequently, sodium gluconate (3 g) and Fe₃O₄ nanoparticles (0.3 g) were dissolved in deionized water (60 mL) under vigorous stirring, and then transferred into a Teflon[®]-lined stainless-steel autoclave with a capacity of 100 mL. The autoclave was sealed and heated at 180 °C for 48 h. After cooling to room temperature, the black products were washed several times with deionized water and absolute ethanol. Finally, the washed precipitate was dried in a vacuum oven at 60 °C for 12 h.

Characterization: The phase structure and phase purity of the as-synthesized products were examined by X-ray diffraction (XRD) by using a Bruker D8 diffractometer with high-intensity Cu-K_α radiation (λ = 1.54 Å). The field-emission scanning electron microscope (SEM) measurements were carried out with a Hitachi S-4800 instrument operating at 15 kV. The samples for SEM were prepared by dispersing the products in ethanol, placing a drop of the solution onto the surface of an Al column, and letting the ethanol evaporate slowly in air. Energy-dispersive X-ray spectroscopy (EDS) mapping with SEM was utilized to determine the elemental distribution. Transmission electron microscopy (TEM) images were taken with a JEOL 2100 transmission electron microscope operated at 200 kV. Fourier transform infrared (FTIR) spectra of all the samples were measured with a Nicolet Nexus 470 spectrometer. Raman spectra were obtained by using a Renishaw Raman system model 2000 spectrometer. XPS measurements were performed with an ESCALAB 250 spectrometer (Thermo-VG Scientific) with Al-K_α X-ray radiation as the X-ray source for excitation. The PL spectra were measured with a Varian Cary Eclipse Fluorescence spectrophotometer. The magnetic properties were measured with a SQUID magnetometer (Lake Shore 7307).

Photochemical Experiments: The photocatalytic activity was evaluated by the degradation of MB under visible light (λ > 420 nm). The visible light was obtained from a 250 W xenon lamp with a 420 nm cutoff filter. A suspension containing powdered catalyst (100 mg) and a fresh aqueous solution of MB (100 mL, 10 mg/L) was magnetically stirred in the dark for ca. 1 h to establish an adsorption-desorption equilibrium for the MB species. The suspensions were kept under constant air-equilibrated conditions before and during illumination. At certain time intervals, 3 mL aliquots were sampled, and the particles were removed. The filtrates were analyzed by recording variations of the maximum absorption band (633 nm) with a UV/Vis spectrophotometer (Shimadzu Corporation, UV-2450).

Supporting Information (see footnote on the first page of this article): SEM image and EDS maps for as-synthesized Bi-MCRCSs, TEM image of Bi-MCRCSs, cycling runs for the photocatalytic degradation of MB in the presence of Bi-MCRCSs.

Acknowledgments

This work was supported by the State Key Laboratory of Urban Water Resource and Environment, Harbin Institute of Technology (grant number HCK201017), Jiangsu Natural Science Fund of China (grant numbers BK2012716, BK20130485), Universities Natural Science Foundation of Jiangsu Province (grant number 11KJB480001), Postdoctoral Foundation of Jiangsu Province (grant number 1102125C), Priority Academic Program Development of Jiangsu Higher Education Institutions (PAPD), and Highly Qualified Professional Initial Funding of Jiangsu University (grant number 10JDG120).

- [1] C. C. Chen, W. H. Ma, J. C. Zhao, *Chem. Soc. Rev.* **2010**, *39*, 4206–4219.
- [2] E. Rodríguez, G. Fernández, B. Ledesma, P. Álvarez, F. J. Beltrán, *Appl. Catal. B* **2009**, *92*, 240–249.
- [3] L. Wang, C. B. Zhang, H. Mestankova, F. Wu, N. S. Deng, G. Pan, M. Bolte, G. Mailhot, *Photochem. Photobiol. Sci.* **2009**, *8*, 1059–1065.
- [4] Q. Lan, F. B. Li, C. S. Liu, X. Z. Li, *Environ. Sci. Technol.* **2008**, *42*, 7918–7923.
- [5] E. M. Rodríguez, B. Núñez, G. Fernández, F. J. Beltrán, *Appl. Catal. B* **2009**, *89*, 214–222.
- [6] M. E. Balmer, B. Sulzberger, *Environ. Sci. Technol.* **1999**, *33*, 2418–2424.
- [7] P. Mazellier, B. Sulzberger, *Environ. Sci. Technol.* **2001**, *35*, 3314–3320.
- [8] F. B. Li, X. Z. Li, C. S. Liu, X. M. Li, T. X. Liu, *Ind. Eng. Chem. Res.* **2007**, *46*, 781–787.
- [9] O. Abida, G. Mailhot, M. Litter, M. Bolte, *Photochem. Photobiol. Sci.* **2006**, *5*, 395–402.
- [10] C. Y. Sun, C. C. Chen, W. H. Ma, J. C. Zhao, *Phys. Chem. Chem. Phys.* **2011**, *13*, 1957–1969.
- [11] P. Cieřła, P. Kocot, P. Mytych, Z. Stasićka, *J. Mol. Catal. A* **2004**, *224*, 17–33.
- [12] L. W. Chen, J. Ma, X. C. Li, J. Zhang, J. Y. Fang, Y. H. Guan, P. C. Xie, *Environ. Sci. Technol.* **2011**, *45*, 3925–3930.
- [13] J. Kochany, *Chemosphere* **1992**, *25*, 261–270.
- [14] Z. J. Luo, H. J. Tang, L. L. Qu, T. T. Han, X. Y. Wu, *Crysol. EngComm* **2012**, *14*, 5710–5713.
- [15] B. Hu, S. H. Yu, K. Wang, L. Liu, X. W. Xu, *Dalton Trans.* **2008**, *40*, 5414–5423.
- [16] B. Hu, K. Wang, L. H. Wu, S. H. Yu, M. Antonietti, M. M. Titirici, *Adv. Mater.* **2010**, *22*, 813–828.
- [17] H. M. Sun, L. Y. Cao, L. H. Lu, *Nano Res.* **2011**, *4*, 550–562.
- [18] M. Sevilla, A. B. Fuertes, *Chem. Eur. J.* **2009**, *15*, 4195–4203.
- [19] Y. J. Cui, J. S. Zhang, G. G. Zhang, J. H. Huang, P. Liu, M. Antonietti, X. C. Wang, *J. Mater. Chem.* **2011**, *21*, 13032–13039.
- [20] Y. Liu, Z. Y. Ren, Y. L. Wei, B. J. Jiang, S. S. Feng, L. Y. Zhang, W. B. Zhang, H. G. Fu, *J. Mater. Chem.* **2010**, *20*, 4802–4808.
- [21] Y. N. Wang, K. J. Deng, L. Z. Zhang, *J. Phys. Chem. C* **2011**, *115*, 14300–14308.
- [22] Y. Ma, C. Zhang, G. Ji, J. Y. Lee, *J. Mater. Chem.* **2012**, *22*, 7845–7850.
- [23] F. Dong, H. Q. Wang, Z. B. Wu, J. F. Qiu, *J. Colloid Interface Sci.* **2010**, *343*, 200–208.
- [24] M. Inagaki, *Carbon* **2012**, *50*, 3247–3266.
- [25] H. J. Huang, D. Z. Li, Q. Lin, W. J. Zhang, Y. Shao, Y. B. Chen, M. Sun, X. Z. Fu, *Environ. Sci. Technol.* **2009**, *43*, 4164–4168.
- [26] Z. H. Wang, W. H. Ma, C. C. Chen, J. C. Zhao, *Environ. Sci. Technol.* **2008**, *42*, 7260–7266.

Received: August 17, 2013

Published Online: January 8, 2014